Optics Letters

Realizing high-efficiency third harmonic generation via accidental bound states in the continuum

Wenjie Tang,[1] Qiming Zhao,[2] Ziyu Wang,[1] Yajun Gao,[1] Jie He,[1] Yi Zhu,[1] Shuxian Wang,[2] Haohai Yu,[2] Ruwen Peng,[1,4] and Mu Wang[1,3,*]

[1]National Laboratory of Solid State Microstructures, School of Physics, and Collaborative Innovation Center of Advanced Microstructures, Nanjing University, Nanjing 210093, China
[2]State Key Laboratory of Crystal Materials and Institute of Crystal Materials, Shandong University, Jinan 250100, China
[3]American Physical Society, Hauppauge, New York 11788, USA
[4]rwpeng@nju.edu.cn
*muwang@nju.edu.cn

Received 30 November 2023; revised 30 January 2024; accepted 31 January 2024; posted 31 January 2024; published 21 February 2024

The bound states in the continuum (BICs) have attracted much attention in designing metasurface due to their high Q-factor and effectiveness in suppressing radiational loss. Here we report on the realization of the third harmonic generation (THG) at a near-ultraviolet wavelength (343 nm) via accidental BICs in a metasurface. The absolute conversion efficiency of the THG reaches 1.13×10^{-5} at a lower peak pump intensity of 0.7 GW/cm^2. This approach allows the generation of an unprecedentedly high nonlinear conversion efficiency with simple structures.

https://doi.org/10.1364/OL.514828

Metasurfaces offer unique opportunities for tailoring the nonlinear response through structural designing and choice of constituent materials [1]. Compared to bulk nonlinear crystals, metasurfaces impose fewer constraints for optical nonlinear harmonic generation, relaxing the phase-matching requirements for nonlinear processes [2]. Metasurfaces can interact with incident light and form high local resonant electromagnetic field intensity via material selection and structural design [3]. For dielectric metasurfaces, the local electromagnetic field can be enhanced by introducing various Mie-type electric and magnetic resonance modes, resulting in high nonlinear conversion efficiency [4–8]. However, due to the energy leakage in conventional Mie-type resonant structures, suppressing radiative losses becomes an important issue. As an alternative approach, achieving high-quality factor (Q-factor) resonances becomes an effective solution [9–11]. It has been known that the bound states in the continuum (BICs) possess extremely high Q-factors and have been recently applied in nonlinear optics [12–16]. BICs are essentially localized wave states that coexist with extended states in the radiating continuum yet without radiation. BICs can be categorized as symmetry-protected BICs and accidental BICs based on their excitation methods [17,18]. Symmetry-protected BICs occur only at the center of the Brillouin zone. The resonant modes of different symmetries are decoupled for the structures with a reflection or rotational symmetry. So when a bound state with a certain symmetry is embedded in the continuum of another symmetry, their coupling is forbidden as long as the symmetry preservation holds [19]. Accidental BICs, however, can occur at nonzero in-plane wave vectors for structures with certain additional symmetries, which originate from the destructive interference of various radiation channels. BICs typically have an infinite Q-factor with vanishing linewidth mathematically, which are non-radiative states confined within the structures and cannot be directly excited by far-field radiation [20].

Unlike symmetry-protected BICs, quasi-BICs with finite but quite high Q-factor can be achieved by breaking structural symmetries in symmetry-protected BICs or tuning parameters in accidental BICs [21–23]. So far, symmetry-protected quasi-BICs have been widely applied to enhance nonlinear signals [13,24–28] and achieve nonlinear circular dichroism [29–32]. However, the Q-factors of symmetry-protected BICs decline rapidly with the vanishing of the symmetry, which is theoretically proportional to α^{-2} (α represents the degree of asymmetry) [33]. The very sensitive dependence of the Q-factors on the structural parameters makes it very challenging for experimental fabrication [24,34]. Yet, it has recently been demonstrated that accidental BICs can be tuned by structural parameters at the center of the Brillouin zone at THz frequencies [35]. The field profile inside the metasurface layer is the superposition of the waves with different propagation constants β_z in the z-direction. Waves from different β_z channels interfere destructively at the interface between the metasurface and free space [36]. Unlike symmetry-protected BICs, accidental BICs are much more tolerant of geometrical inaccuracy and are easier to fabricate [35,37,38]. Accidental BICs have gained significant interest in recent years due to their potential applications in photonics, quantum information processing, and energy harvesting devices [39–41].

In this Letter, we present a metasurface supporting both symmetry-protected BIC and accidental BIC modes. In accidental BIC with α around 0.21, the metasurface maintains a resonance with a high Q-factor in a broad range of structural parameters. By changing the asymmetry parameter, we experimentally fabricate the silicon metasurfaces with various length parameters of the nanopillars and measure the reflectance spectrum in the vicinity of the fundamental wavelength (1030 nm)

Table 1. Comparison of the Experimentally Measured THG Efficiency from Si Metasurfaces

Reference	THG Wavelength	Peak Pump Intensity	Efficiency
Nano Lett. 14, 6488 (2014). [6]	420 nm	~5.5 GW/cm^2	~10^{-7}
Nano Lett. 15, 7388 (2015). [9]	449 nm	~3.2 GW/cm^2	1.2×10^{-6}
Nano Lett. 18, 8054 (2018). [7]	467 nm	~33 GW/cm^2	1.1×10^{-6}
ACS Photonics 5, 1671 (2018). [8]	427 nm	~0.5 GW/cm^2	1.76×10^{-7}
ACS Photonics. 6, 1639 (2019). [24]	477 nm	~2.6 GW/cm^2	~10^{-6}
Phys. Rev. Lett. 123, 25390 (2019). [13]	528 nm	0.1 GW/cm^2	0.9×10^{-6}
Nano Lett. 22, 2001 (2022). [25]	417 nm	0.4 GW/cm^2	1.8×10^{-6}
Light: Sci. Appl. 12, 97 (2023). [26]	520 nm	1.2 GW/cm^2	2.8×10^{-7}
Adv. Optical Mater. 11,2300526(2023). [10]	427 nm	23.3 GW/cm^2	2.2×10^{-6}
This work	343 nm	0.7 GW/cm^2	1.13×10^{-5}

and the nonlinear optical response of the designed metasurfaces in the NUV regime (343 nm). We achieve an enhancement of the THG up to 1.13×10^{-5} at a low peak pump intensity of 0.7 GW/cm^2 with $\alpha=0.21$. To the best of our knowledge, this is the highest THG efficiency achieved at this level of pump intensity, as listed in Table 1. With the same strategy, selecting a material with lower optical absorption (such as TiO_2) to enhance THG signals at shorter wavelengths is possible. We expect this approach will enlighten the generation of harmonic waves in the vacuum ultraviolet (VUV) regime.

We designed a nano-cuboid metasurface of the amorphous silicon, as shown in Fig. 1(a). The unit cell of the metasurface consists of two cuboid structures with different lengths and is arranged in a square lattice with lattice constant P. The geometrical parameters of the cuboids, W, H, L, and L-Δl, are defined in Fig. 1(a). The asymmetry of the unit cell is featured by the length difference Δl. We define a dimensionless parameter $\alpha=\Delta l/L$ to characterize the asymmetry. We simulate the linear resonance of the structure and its eigenmodes using the finite element method (COMSOL Multiphysics v. 5.6). The periodic boundary conditions are introduced in the x- and y-direction boundaries, and the perfectly matched layer conditions are applied in the z-direction. The refractive index of the amorphous silicon is experimentally measured as 3.55. The resonant wavelength of the structure is tuned to 1030 nm by selecting $P=450$ nm, $L=390$ nm, $W=120$ nm, and $H=400$ nm. The neighboring cuboids L1 and L2 in the unit cell are separated at 105 nm.

Figure 1(b) illustrates the evolution of the reflectance spectra of the metasurfaces near 1030 nm with α ranging from 0 to 0.5 for the x-polarized normal incidence. For the scenario that

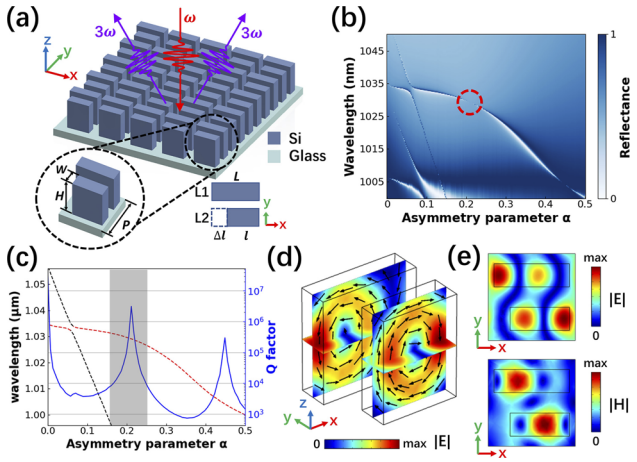

Fig. 1. (a) Schematic shows the metasurface structures, where the asymmetric unit cell consists of two cuboids with different lengths. (b) Reflectance under the incidence of polarized light in the x-direction versus asymmetry parameter α (horizontal axis) and wavelength (vertical axis). (c) Q-factor (blue solid line) of the designed BIC and eigenmode wavelength (dashed line) as a function of α. (d) Electric field inside the two Si cuboids for the accidental BIC when α is around 0.21. The electric field vector is shown with black arrows. (e) Near-field distributions of the electric and magnetic fields of the accidental BIC when α is around 0.21.

two rectangular nanopillars are identical ($\alpha=0$), the metasurface supports a BIC protected by the in-plane twofold rotational symmetry of the unit cell. The reflectance spectrum has no sharp resonance peak due to the complete decoupling of the BIC mode from the radiation continuum. Once a nonzero α emerges, the symmetry of the unit cell is broken, and the metasurface transforms into a quasi-BIC mode supporting a high Q-factor. With the increase of α, the quasi-BIC mode gradually shifts toward shorter wavelengths. However, further increase of α leads to the vanished linewidth or resonance peaks in the reflectance spectrum near $\alpha=0.21$ [marked by the red circle in Fig. 1(b)] and $\alpha=0.45$. It means that there is no outgoing power. Therefore, a non-radiative state occurs at these two α values. Meanwhile, the significantly enhanced electric field inside the silicon metasurface generates the nonlinear optical effect of the THG.

The dashed lines in Fig. 1(c) show the eigenmode wavelength as a function of α via the eigenmode analysis in COMSOL calculations. We highlight the designed BIC mode in red, which couples to another mode (black dashed line) when α is around 0.06. It can be seen that the eigenmode wavelength is consistent with the reflectance spectra in Fig. 1(b). The solid line in Fig. 1(c) illustrates the Q-factor of the designed BIC as a function of α, where the Q-factor is defined as $Q=\mathrm{Re}(\omega)/2\mathrm{Im}(\omega)$. In the solid line in Fig. 1(c), the Q-factor has a local maximum around $\alpha=0.21$ and 0.45, respectively, corresponding to the accidental BIC, which are in good agreement with the reflectance spectra in Fig. 1(b). As shown in the shaded area in Fig. 1(c), the Q-factor remains larger than 10^4 as α keeps between 0.15 and 0.25. Compared to the symmetry-protected BIC ($\alpha=0$), accidental BIC provides a much wider range of geometrical parameters (α around 0.21) with a high Q-factor. Technically, this feature is extremely favorable for fabrication since it provides a high tolerance to the errors of the geometrical parameters of nanopillars. The electric and magnetic field profiles around $\alpha=0.21$ are

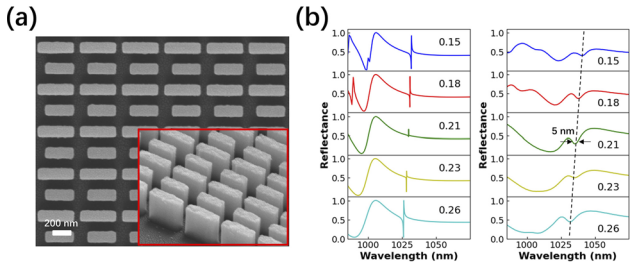

Fig. 2. (a) Top view and 45° tilted-angle (inset) SEM images of the fabricated Si metasurface placed on a fused silica substrate. (b) Evolution of the simulated (left) and measured (right) reflectance spectra versus asymmetry parameter α (0.15, blue; 0.18, red; 0.21, green; 0.23, yellow; 0.26, cyan).

shown in Figs. 1(d) and 1(e). The black arrows show the electric field vectors in the x–z plane in Fig. 1(d). Two oppositely loop-shaped electric fields in the x–z plane are formed in two nanopillars corresponding to two magnetic dipoles oppositely oriented in the y-direction, respectively. The slight dissimilar amplitudes and space misalignment between the two magnetic dipoles arise from the broken symmetry, as shown in Fig. 1(e). It can be seen from the field profiles that the metasurface possesses a strong electric field buildup inside the nanopillars corresponding to the accidental BIC mode, which effectively enhances the nonlinear signals.

Experimentally, we fabricate the silicon metasurfaces with different asymmetry parameters α, and the area of the metasurface is $100\,\mu m \times 100\,\mu m$. We first deposit a layer of an amorphous silicon, 400 nm in thickness, on a fused silica substrate by plasma-enhanced chemical vapor deposition (PECVD). Then, a layer of photoresist is spin-coated on the substrate. Electron beam lithography (EBL) defines the designed pattern on the sample. After development, an inverse pattern is formed on the photoresist layer. A 30-nm-thick Al_2O_3 layer is then deposited on the sample by electron beam evaporation. We apply the chemical lift-off technique by soaking the sample in a resist remover to peel off the photoresist layer. After this process, only the desired Al_2O_3 patterns survive on the amorphous silicon layer. After that, we use the inductively coupled plasma reactive ion etching (ICP-RIE) with C_4F_8 (40 SCCM) and SF_6 (30 SCCM), to etch the silicon film. Finally, a metasurface with Si cuboid structures is fabricated by removing the remaining Al_2O_3 mask with dilute hydrochloric acid.

Figure 2(a) demonstrates the micrographs of the top and 45°-side view of the fabricated metasurface with field-emission scanning electron microscopy (FESEM). Figure 2(b) illustrates the simulated (left) and experimentally measured (right) reflectance spectra with α varying from 0.15 to 0.26 in x-polarized normal incidence. Different values of α are shown in each plot. It can be seen that the excited quasi-BIC resonance blueshifts continuously near 1030 nm with increasing α, which is in good agreement with the numerical simulations. The full width at half maximum (FWHM) of the quasi-BIC resonance is around 5 nm at α=0.21, corresponding to a Q-factor of 206. Comparing the reflectance spectra with other values of α in Fig. 2(b), the Q-factor of the resonance drops a little as α deviates from 0.21 to both sides. Compared to the simulated Q-factors ($>10^4$), the experimentally measured value is much smaller, which may be induced by the errors in sample fabrication. The linewidth of resonance peaks in the reflectance spectra, however, does not deviate obviously as α changes.

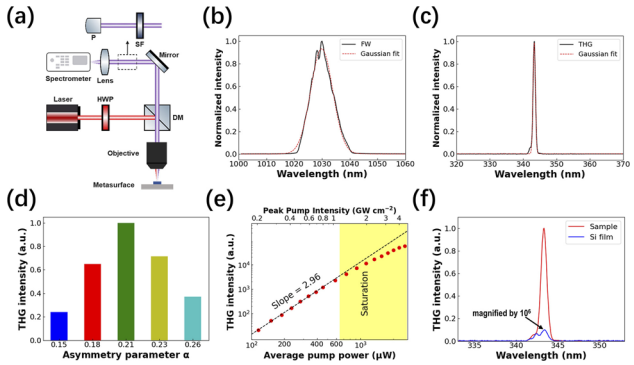

Fig. 3. (a) Schematics of the experimental setup to measure the THG reflectance. HWP, half-wave plate; DM, dichroism mirror; SF, short pass filter; P, powermeter. (b) Normalized spectrum of the fundamental pump laser (c) Normalized spectrum of the THG signal generated from the Si metasurface. The dashed red lines in (b) and (c) show the Gaussian curve fitting. (d) Experimentally measured dependence of the THG intensity with respect to the asymmetry parameter α. (e) Log–log plot of the output THG power as the function of the average pump power and the peak pump intensity for the Si metasurface with $\alpha = 0.21$. The red dots show the measured data and the black dashed line is a numerical fit with a third-order power function. The yellow area covers the pump power range where the cubic law has been deviated. (f) Measured THG enhancement of the Si metasurface with respect to the signal from an unpatterned silicon film (magnified by 10^6 times).

Figure 3(a) shows the experimental setup to measure the THG of the silicon metasurfaces. A femtosecond laser (BWT BFL-1030-10H; wavelength, 1030 nm; repetition frequency, 100 kHz; and pulse width, 200 fs) outputs an x-polarized pump beam. The pump beam that passes through a half-wave plate is reflected by a dichroic mirror and focuses on the sample via a 10× objective (NA = 0.25). The diameter of the focus spot is 60 μm. The THG signal generated on the sample is collected by the same objective lens in the reflection mode and analyzed by a spectrometer (HORIBA iHR550). A powermeter with filters is applied to measure the THG intensity quantitatively. Figures 3(b) and 3(c) show the normalized spectra of the fundamental laser and THG signal, respectively, where the dashed red lines show the Gaussian curve fitting. The bandwidth of the THG is much narrower than that of the fundamental pump laser. In Fig. 3(d), we compare the THG signals from the samples with different asymmetry parameters α varying from 0.15 to 0.26. The THG signal reaches the maximum at $\alpha = 0.21$. Meanwhile, with incident average pump power of 0.4 mW, the absolute conversion efficiency η, which is defined as $\eta = P_{THG}/P_{FW}$ with P_{THG} and P_{FW} representing the THG power and fundamental pump power, respectively, reaches 1.13×10^{-5} at the peak pump intensity of $0.7\,GW/cm^2$. The dependence of the THG and pump power is illustrated in Fig. 3(e). From the fitting dashed line, one may find that the power of harmonic generation has a cubic relation with respect to the pump power, indicating the occurrence of the third harmonic generation. When the average pump power exceeds 0.4 mW, the saturation becomes evident. As a comparison, we measure the spectra of the THG signal from the metasurface at $\alpha = 0.21$ and an unpatterned flat silicon film, as illustrated in Fig. 3(f). It turns out that the THG generated on the metasurface is about seven orders of magnitude larger than that generated on a flat silicon film with the same thickness.

The absorption of the amorphous silicon consumes ~89.4% of the THG power in the transmission process, which is calculated by COMSOL simulations with and without silicon absorption at 343 nm. Further, in our current experimental setup, some nonlinear signals with larger diffraction angles are not collected due to the small numerical aperture of the objective lens (NA = 0.25). With COMSOL simulations, we estimate that only ~46.4% of the total reflection THG power is collected by the objective lens in our experiment. The peak pump intensity can be expressed as $I_{peak} = P_{avg}/(\Delta t \cdot f \cdot A)$, where P_{avg} is the incident average pump power, Δt is the pulse width, f is the repetition rate, and A is the focus point area on the sample. A is inversely proportional to the square of the numerical aperture of the objective lens. For the safety of the sample, I_{peak} needs to be confined in a certain range as a constant. So, the efficiency could be boosted by using an objective lens with a large numerical aperture and introducing a higher repetition frequency pump laser. Besides, the doubly resonant strategy [42,43] has been theoretically proposed to enhance harmonic conversion efficiency. In our system, we have not yet found a clue that this mechanism plays a role. Yet, it is always exciting to explore different ways to boost the THG efficiency.

We should point out that in our experiment, the fundamental wavelength is 1030 nm, and the THG output wavelength is 343 nm. It is interesting to explore the possibility of achieving harmonic generations with even shorter wavelengths. For materials like amorphous silicon, the absorption loss is significant when the pump laser wavelength approaches the visible regime. The materials with less absorption at the visible wavelength, such as TiO_2, may generate a THG in the VUV band [44,45]. The UV absorption edge of TiO_2 is 400 nm, corresponding to its bandgap of ~3.1 eV [46]. It is possible to apply our design to TiO_2 and generate a THG signal with a shorter wavelength in the vacuum ultraviolet regime. The detection of the VUV light requires an ultrahigh vacuum environment to prevent the absorption of the VUV light by oxygen. Besides, the optical system, including the substrate, should be replaced by VUV-transparent materials, such as CaF_2 and MgF_2 [47].

To summarize, we design a silicon metasurface supporting accidental BICs with high tolerance to fabrication errors. Using this approach, we experimentally achieved the enhancement of the THG on the silicon metasurface. A significant THG conversion efficiency of 10^{-5} is measured at 343 nm at a lower peak pump intensity of 0.7 GW/cm^2. The THG signal measured from the silicon metasurface is enhanced by a factor of ~10^7 compared to an unpatterned silicon film with the same thickness. We also explored the possibility of using TiO_2 to replace silicon to generate efficient THG signals at shorter wavelengths theoretically. This strategy looks promising for many applications, such as biosensing, material characterization, photolithography, and high-resolution photoelectron spectroscopy in ultraviolet regimes.

Funding. National Natural Science Foundation of China (11974177, 12234010, 61975078); National Key Research and Development Program of China (2022YFA1404303, 2020YFA0211300).

Disclosures. The authors declare no conflicts of interest.

Data availability. The data that support the findings of this study are available from the corresponding authors upon reasonable request.

REFERENCES

1. G. Li, S. Zhang, and T. Zentgraf, Nat. Rev. Mater. **2**, 17010 (2017).
2. A. Krasnok, M. Tymchenko, and A. Alù Mater, Mater. Today **21**, 8 (2018).
3. M. W. Klein, C. Enkrich, M. Wegener, *et al.*, Science **313**, 502 (2006).
4. Y. Kivshar, Natl. Sci. Rev. **5**, 144 (2018).
5. K. Koshelev, G. Favraud, A. Bogdanov, *et al.*, Nanophotonics **8**, 725 (2019).
6. M. R. Shcherbakov, D. N. Neshev, B. Hopkins, *et al.*, Nano Lett. **14**, 6488 (2014).
7. Y. Gao, Y. Fan, Y. Wang, *et al.*, Nano Lett. **18**, 8054 (2018).
8. S. Chen, M. Rahmani, K. F. Li, *et al.*, ACS Photonics **5**, 1671 (2018).
9. Y. Yang, W. Wang, A. Boulesbaa, *et al.*, Nano Lett. **15**, 7388 (2015).
10. A.-Y. Liu, J.-C. Hsieh, K.-I. Lin, *et al.*, Adv. Opt. Mater. **11**, 2300526 (2023).
11. H. Liu, C. Guo, G. Vampa, *et al.*, Nat. Phys. **14**, 1006 (2018).
12. K. Koshelev, S. Kruk, E. Melik-Gaykazyan, *et al.*, Science **367**, 288 (2020).
13. Z. Liu, Y. Xu, Y. Lin, *et al.*, Phys. Rev. Lett. **123**, 253901 (2019).
14. L. Carletti, K. Koshelev, C. De Angelis, *et al.*, Phys. Rev. Lett. **121**, 033903 (2018).
15. S. Xiao, M. Qin, J. Duan, *et al.*, Phys. Rev. B **105**, 195440 (2022).
16. S. Feng, T. Liu, W. Chen, *et al.*, Sci. China Phys. Mech. Astron. **66**, 124214 (2023).
17. M.-S. Hwang, K.-Y. Jeong, J.-P. So, *et al.*, Commun. Phys. **5**, 106 (2022).
18. D. Zografopoulos and O. Tsilipakos, Mater. Adv. **4**, 11 (2023).
19. C. W. Hsu, B. Zhen, A. D. Stone, *et al.*, Nat. Rev. Mater. **1**, 16048 (2016).
20. K. Koshelev, A. Bogdanov, and Y. Kivshar, Opt. Photonics News **31**, 38 (2020).
21. Y. Plotnik, O. Peleg, F. Dreisow, *et al.*, Phys. Rev. Lett. **107**, 183901 (2011).
22. E. Melik-Gaykazyan, K. Koshelev, J.-H. Choi, *et al.*, Nano Lett. **21**, 1765 (2021).
23. P. Vabishchevich and Y. Kivshar, Photonics Res. **11**, B50 (2023).
24. K. Koshelev, Y. Tang, K. Li, *et al.*, ACS Photonics **6**, 1639 (2019).
25. G. Yang, S. U. Dev, M. S. Allen, *et al.*, Nano Lett. **22**, 2001 (2022).
26. D. Hähnel, C. Golla, M. Albert, *et al.*, Light: Sci. Appl. **12**, 97 (2023).
27. S. Xiao, M. Qin, J. Duan, *et al.*, Opt. Express **30**, 32590 (2022).
28. A. P. Anthur, H. Zhang, R. Paniagua-Dominguez, *et al.*, Nano Lett. **20**, 8745 (2020).
29. M. Gandolfi, A. Tognazzi, D. Rocco, *et al.*, Phys. Rev. A **104**, 023524 (2021).
30. Y. Chen, H. Deng, X. Sha, *et al.*, Nature **613**, 474 (2023).
31. T. Shi, Z. L. Deng, G. Geng, *et al.*, Nat. Commun. **13**, 4111 (2022).
32. M. V. Gorkunov, A. A. Antonov, and Y. S. Kivshar, Phys. Rev. Lett. **125**, 093903 (2020).
33. K. Koshelev, S. Lepeshov, M. Liu, *et al.*, Phys. Rev. Lett. **121**, 193903 (2018).
34. F. Yesilkoy, E. R. Arvelo, Y. Jahani, *et al.*, Nat. Photonics **13**, 390 (2019).
35. S. Han, P. Pitchappa, W. Wang, *et al.*, Adv. Opt. Mater. **9**, 2002001 (2021).
36. C. W. Hsu, B. Zhen, J. Lee, *et al.*, Nature **499**, 188 (2013).
37. B. Wang, J. Liu, J. Liu, *et al.*, J. Appl. Phys. **133**, 023103 (2023).
38. J. Niu, Y. Zhai, Q. Han, *et al.*, Opt. Lett. **46**, 162 (2021).
39. M. Sidorenko, O. Sergaeva, Z. Sadrieva, *et al.*, Phys. Rev. Appl. **15**, 034041 (2021).
40. D. R. Abujetas, J. Olmos-Trigo, and J. A. Sánchez-Gil, Adv. Opt. Mater. **10**, 2200301 (2022).
41. M. Kang, S. Zhang, M. Xiao, *et al.*, Phys. Rev. Lett. **126**, 117402 (2021).
42. H. Hashemi, A. W. Rodriguez, J. Joannopoulos, *et al.*, Phys. Rev. A **79**, 013812 (2009).
43. T. Christopoulos, E. E. Kriezis, and O. Tsilipakos, Phys. Rev. B **107**, 035413 (2023).
44. S. Y. Kim, Appl. Opt. **35**, 6703 (1996).
45. M. Semmlinger, M. Zhang, M. L. Tseng, *et al.*, Nano Lett. **19**, 8972 (2019).
46. C. C. Evans, K. Shtyrkova, O. Reshef, *et al.*, Opt. Express **23**, 7832 (2015).
47. T. Jia, H. Chen, M. Huang, *et al.*, Phys. Rev. B **73**, 054105 (2006).